Astronomy & Astrophysics manuscript no. 42036corr_final
October 11, 2021

High resolution LAsMA ^{12}CO and ^{13}CO observation of the G305 giant molecular cloud complex : II. Effect of feedback on clump properties ⋆

P. Mazumdar[1], F. Wyrowski[1], J. S. Urquhart[2], D. Colombo[1], K. M. Menten[1], S. Neupane[1], and M. A. Thompson[3]

[1] Max-Planck-Institut für Radioastronomie, Auf dem Hügel 69, 53121 Bonn, Germany
e-mail: pmazumdar@mpifr-bonn.mpg.de
[2] Centre for Astrophysics and Planetary Science, University of Kent, Canterbury, CT2 7NH, UK
[3] Centre for Astrophysics Research, Science and Technology Research Institute, University of Hertfordshire, College Lane, Hatfield AL10 9AB, UK

Received xxx / Accepted xxx

ABSTRACT

Context. Understanding the effect of feedback from young massive stars on the star-forming ability of their parental molecular clouds is of central importance for studies of the interstellar medium and star formation.
Aims. We observed the G305 star-forming complex in the J = 3-2 lines of ^{12}CO and ^{13}CO to investigate whether feedback from the central OB stars was triggering star formation in G305 or actually disrupting this process.
Methods. The region was decomposed into clumps using dendrogram analysis. A catalog of the clump properties such as their positions, luminosities, masses, radii, velocity dispersions, volume densities, and surface mass densities was created. The surface mass densities of the clumps were plotted as a function of the incident 8 μm flux. A mask of the region with 8 μm flux > 100 MJy/sr was created and clumps were categorized into three classes based on their extent of overlap with the mask, namely mostly inside (>67% overlap), partly inside (>10% and <67% overlap), and outside (<10% overlap). The surface mass density distribution of each of these populations was separately plotted. This was followed by comparing the G305 clumps with the Galactic average taken from a distance-limited sample of ATLASGAL and CHIMPS clumps. Finally, the cumulative distribution functions (CDFs) of the clump masses in G305 and their L/M ratios were compared to that of the Galactic sample to determine which mechanism of feedback was dominant in G305.
Results. The surface mass densities of clumps showed a positive correlation with the incident 8 μm flux. The data did not have sufficient velocity resolution to discern the effects of feedback on the linewidths of the clumps. The subsample of clumps labeled mostly inside had the highest median surface mass densities followed by the partly inside and outside subsamples. The difference between the surface mass density distribution of the three subsamples were shown to be statistically significant using the Kolmogorov–Smirnov (KS) test. The mostly inside sample also showed the highest level of fragmentation compared to the other two subsamples. These prove that the clumps inside the G305 region are triggered. The G305 clump population is also statistically different from the Galactic average population, the latter approximating that of a quiescent population of clumps. This provided further evidence that redistribution was not a likely consequence of feedback on the giant molecular cloud (GMC). The CDFs of clump masses and their L/M ratios are both flatter than that of the Galactic average, indicating that clumps are heavier and more efficient at forming stars in G305 compared to the Galactic average.
Conclusions. Feedback in G305 has triggered star formation. The collect and collapse method is the dominant mechanism at play in G305.

Key words. Submillimeter: ISM – ISM:structure – ISM: evolution – Stars: formation – methods: analytical – techniques: image processing

1. Introduction

G305 is one of the most massive and luminous star-forming giant molecular clouds (GMCs) in the Milky Way (Clark & Porter (2004), Fig. 1). It is located ∼ 4 kpc (Clark & Porter 2004; Davies et al. 2012; Borissova et al. 2019) away from us at $l \sim 305°$, $b \sim 0°$ in the Scutum-Crux spiral arm of the Galactic plane. Its center has been cleared of the interstellar molecular gas by the stellar winds and the ionizing front originating from massive stars belonging to two visible central clusters (Danks 1 and 2) consisting of 21 OB stars and a Wolf-Rayet star (WR48a) (Clark & Porter 2004; Davies et al. 2012). A diffuse population of evolved massive stars has been found to exist inside the cavity with ages similar to that of the two clusters (Leistra et al. 2005; Shara et al. 2009; Mauerhan et al. 2011; Davies et al. 2012; Faimali et al. 2012; Borissova et al. 2019). The central cavity is also filled with ionized gas as shown by radio continuum observations by Hindson et al. (2012). Surrounding the central cavity is a thick layer of molecular gas (Hindson et al. 2010, 2013; Mazumdar et al. 2021). Multiple studies have reported star formation tracers: water and methanol masers, HII and ultracompact (UC) HII regions, and massive young stellar objects (MYSOs) (Clark & Porter 2004; Hindson et al. 2012;

⋆ Full version of Table 1 is only available in electronic form at the CDS via anonymous ftp to cdsarc.u-strasbg.fr (130.79.128.5) or via http://cdsweb.u-strasbg.fr/cgi-bin/qcat?J/A+A/

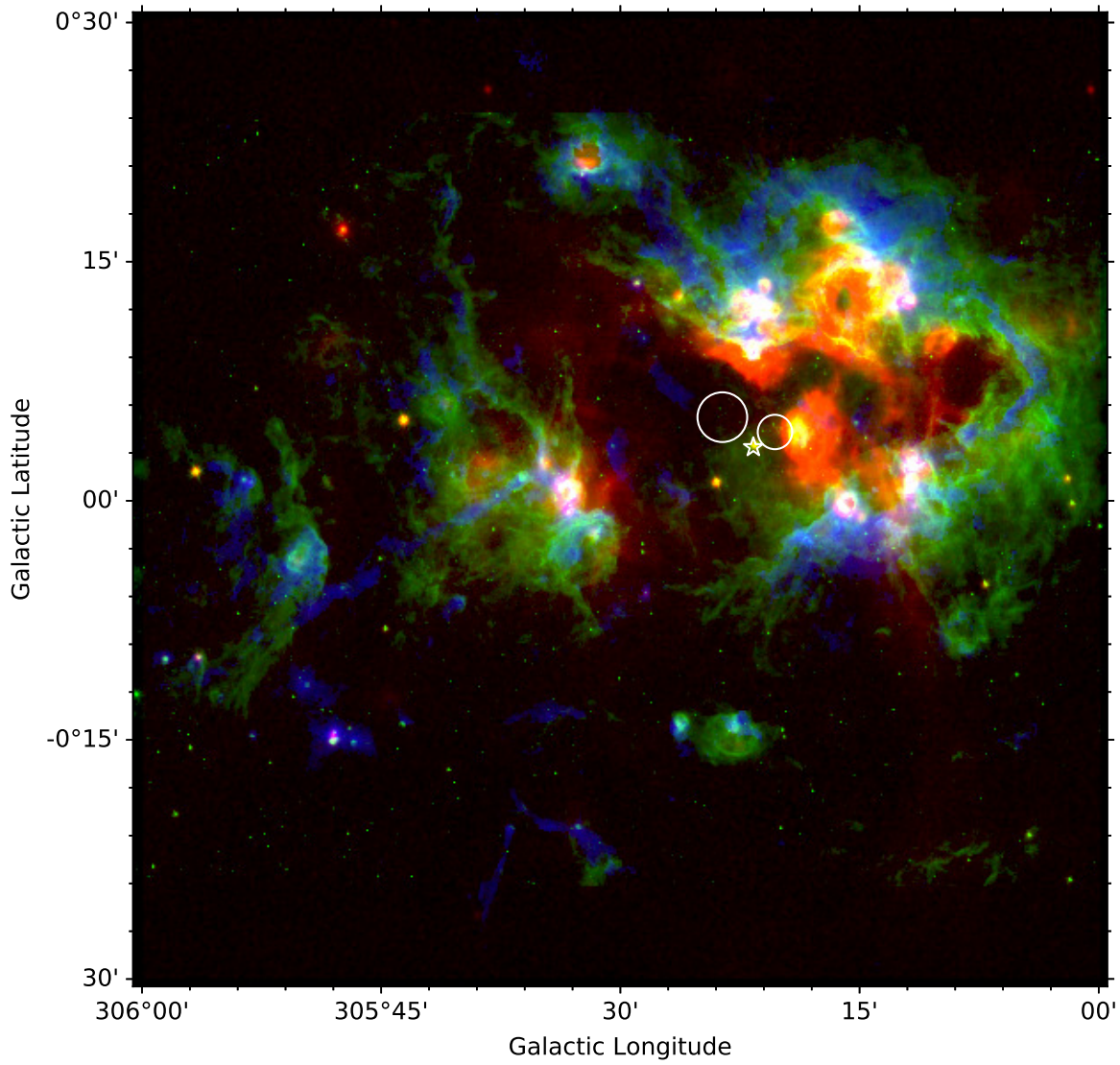

Fig. 1. Three-color image (green = *Spitzer*-IRAC4 8 μm, red = Midcourse Space Experiment (MSX) 21.3 μm, blue = LAsMA (^{13}CO(3-2) moment-0)) of the G305 star-forming complex. The 21.3 μm emission is dominated by hot dust in the HII region. The colder gas is traced by the ^{13}CO(3-2) line emission. The interface between the ionized and molecular gas appears as a blend of green (strong 8 μm emission from PAHs), blue (colder molecular gas), and occasionally red (interfaces very close to HII regions). The positions of the Danks 1 and 2 clusters are given by the smaller and the larger white circles, respectively, and WR48a is shown as a white star.

Lumsden et al. 2013; Urquhart et al. 2014a; Green et al. 2009, 2012). Figure 1 shows a three-color composite image of G305 highlighting three aspects of the complex. The 21.3 μm Midcourse Space Experiment (MSX) (Price et al. 2001) image is shown in red and traces the hot dust being heated by the OB stars within the cavity and towards the edges where the ionization front is interacting with the surrounding molecular gas. The cold molecular gas traced by the integrated ^{13}CO (3−2) line emission (Mazumdar et al. 2021, hereafter Paper I) can be seen in blue being shrouded by emission from the 8 μm filter of the Spitzer Infrared Array Camera (IRAC) (Churchwell et al. 2009) shown in green. The IRAC traces the polycyclic aromatic hydrocarbons (PAHs) whose emission is excited by the far-UV photons emanating from the stars in the central cavity.

The role played by feedback from high mass stars (M > 8 $M_\odot$) on their surrounding interstellar medium (ISM) has been a subject of active research. As is the case in G305, these stars exist in massive clusters located inside GMCs (Motte et al. 2018). They inject energy and momentum into their natal clouds via very strong stellar winds, ionizing radiation and eventually supernovae (Krumholz et al. 2014). Such feedback from OB stars can potentially enhance and/or disrupt the formation of subsequent generations of stars (Krumholz et al. 2014; Deharveng et al. 2010), consequently playing a vital role in the evolution of GMCs (Zinnecker & Yorke 2007). The G305 region, being a very extensively studied GMC, is a very good candidate to examine the effects of feedback on the GMC. Although circumstantial evidence of triggering in G305 exists (Clark & Porter 2004; Hindson et al. 2010), it has, as yet, not been definitively proven.

Having investigated the effects of feedback on the GMC as a whole, we are now interested in exploring the effects of feedback on the ability of the GMC to form subsequent generations of stars. GMCs show a hierarchical structure with clouds condensing into clumps that condense and fragment into cores, eventually forming stars (Blitz & Stark 1986; Lada 1992). Since clumps provide the environment and the raw material for star formation,

the impact of feedback on the future generation of stars can be studied by their effect on the clump properties in a GMC. In this paper we decompose the molecular emission distribution in G305 into clumps and investigate their properties in an effort to study how feedback has affected clump properties and whether the observed star formation has been triggered.

A broad classification of the effects of feedback on star formation can lead to three different scenarios which we outline here:

Redistribution: The expansion of an HII region simply moves the star-forming clumps to its edge. The molecular cloud is already seeded with dense clumps that would collapse to form stars. An apparent enhancement of star formation observed on the periphery of the HII region is not necessarily caused by the HII region. However, overall star formation has not been enhanced. We call this the redistribution scenario.

Dispersion: In high mass star-forming regions feedback is very strong and can simply disperse most of the molecular material via various mechanisms (Krumholz et al. 2014, and references therein), thereby suppressing the ability of the GMC to form stars. We call this the dispersion scenario.

Triggering: In this case the feedback from the stars actually enhances or induces star formation in the natal cloud. Many mechanisms are known or hypothesized to be responsible for triggering, e.g., supernovae (de Geus 1992; Nagakura et al. 2009, and references therein), cloud-cloud collisions (for a comprehensive review, see Fukui et al. 2021), collect and collapse (C&C) processes (Elmegreen & Lada 1977; Dale et al. 2007), and radiation driven implosions (RDI) (Bertoldi 1989; Bertoldi & McKee 1990; Kessel-Deynet & Burkert 2003; Lee & Chen 2007). In G305, there has been an indication of the C&C mechanism playing a role in triggering star formation (Hindson et al. 2010). The C&C model was first proposed by Elmegreen & Lada (1977). In this scenario the expanding warm ionized gas sweeps up a shell of shocked cool neutral gas. This compressed and shocked layer may become gravitationally unstable along its surface on a long timescale. This process allows massive dense fragments to form, which quickly fragment in turn leading to the formation of a cluster of stars of roughly the same age (Whitworth et al. 1994; Deharveng et al. 2005). We therefore concentrate our efforts on testing this specific triggering mechanism in G305.

In this paper we aim to find out which of the three scenarios mentioned above is dominant. Based on observations of NH_3 inversion lines, Hindson et al. (2010) found the concentration of star formation tracers in G305 to be enhanced inside a clump that faces the ionizing sources. The analysis presented in (Hindson et al. 2010) is consistent with a triggering scenario, but the evidence is circumstantial. In order to robustly determine which of the three scenarios presented above dominates, we need to study the statistical properties of clumps, especially those related to star-forming properties of the clumps (e.g., their masses, luminosity to mass ratios, surface mass densities). If the feedback is simply moving the clumps around, there should not be any significant difference in the mass distribution function of the clumps in G305 when compared to the Galactic average. For the dispersion case we expect to see fewer clumps and fewer massive clumps. And finally, if triggering is dominant, we expect to see more massive clumps when compared to the Galactic average and, in case of an increased star-forming efficiency, a higher luminosity-to-mass ratio.

We discuss the observations and methods of data reduction in Sect. 2. In Sect. 3 we introduce the ancillary survey data used to aid our analysis. Sections 4 and 5 explains the details of the clump extraction method and how their properties were estimated. Sect. 6 explores the effect feedback has on certain clump properties and how this may support or reject different scenarios presented in this section. In Sect. 7 we compare the properties of G305 clumps with the average Galactic sample to provide support for one of the three scenarios. Finally, Sect. 8 presents the summary of our findings.

2. Observations and data reduction

The Atacama Pathfinder Experiment (APEX) (Güsten et al. 2006) telescope[1] was used to observe the 1 degree squared region spanning a longitude range $305° < l < 306°$ and latitude $-0.5° < b < 0.5°$. The Large APEX sub-Millimeter Array (LAsMA) receiver (Güsten et al. 2008) was used to observe the $J = 3 - 2$ transitions of ^{12}CO ($\nu_{\rm rest} \sim 345.796$ GHz) and ^{13}CO ($\nu_{\rm rest} \sim 330.588$ GHz) simultaneously. The observations were done under project number M-099.F-9527A-2017.

The details of the observations, calibrations as well as data reduction have been described in Paper I. Here we briefly summarize the whole process. The local oscillator frequency was set at 338.190 GHz in order to avoid contamination of the ^{13}CO (3-2) lines due to bright ^{12}CO (3-2) emission from the image band. The whole region was observed using a position switching on-the-fly (OTF) technique in perpendicular directions in order to avoid systematic scanning effects. The data was calibrated using a three-load chopper wheel method, which is an extension of the standard method used for millimeter observations (Ulich & Haas 1976) to calibrate the antenna temperature T_A^* scale. The data were reduced using the GILDAS package[2]. Baseline subtraction was done on each spectrum after masking the velocity range -150 km s^{-1} to 50 km s^{-1} in order to avoid fitting emission features. The average of all the spectra was then used to mask the channels containing line emissions, and baseline fitting was repeated to obtain a cleaner and flatter baseline. The resulting reduced spectra were then gridded with a 6″ cell (hereafter referred to as a pixel) and convolved with a Gaussian kernel with a full width at half maximum (FWHM) size of one-third the telescope FWHM beam width. The final data cube has a spatial resolution of $\sim$ 20″, and a velocity resolution of 0.5 km s^{-1}. In order to obtain the rms noise, the standard deviation was calculated over a range of 100 emission-free spectral channels for each pixel. Figure 2 shows the distribution of the noise in the G305 region for the ^{12}CO and ^{13}CO lines. The noise distribution peaks at 0.13 K for ^{12}CO and 0.29 K for ^{13}CO . These values were therefore adopted to be the rms noise (hereafter σ_{noise}) for each map.

3. Ancillary data

In order to compare and analyze G305 clump properties with the Galactic clumps, we used the clump catalogs from the ATLAS-

[1] This publication is based on data acquired with the Atacama Pathfinder EXperiment (APEX). APEX is a collaboration between the Max-Planck-Institut für Radioastronomie, the European Southern Observatory, and the Onsala Space Observatory.

[2] http://www.iram.fr/IRAMFR/GILDAS

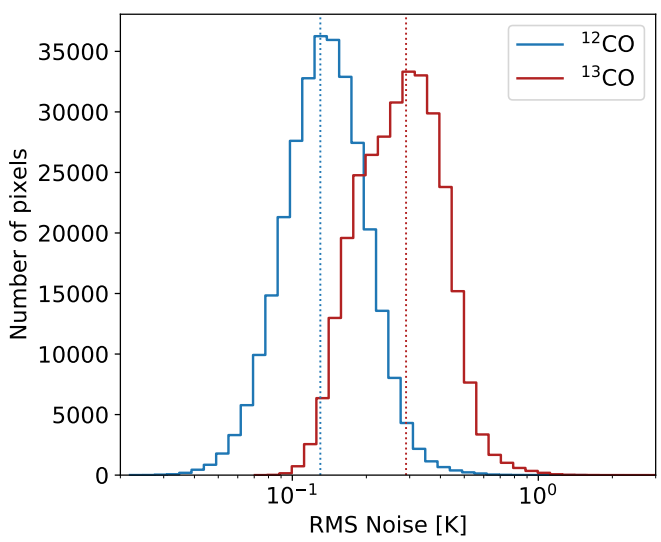

Fig. 2. Histogram distribution of rms noise values for the LAsMA map of the G305 region. The ^{12}CO map distribution peaks at 0.13 K and that of ^{13}CO peaks at 0.29 K, as indicated by the blue and red dotted lines, respectively.

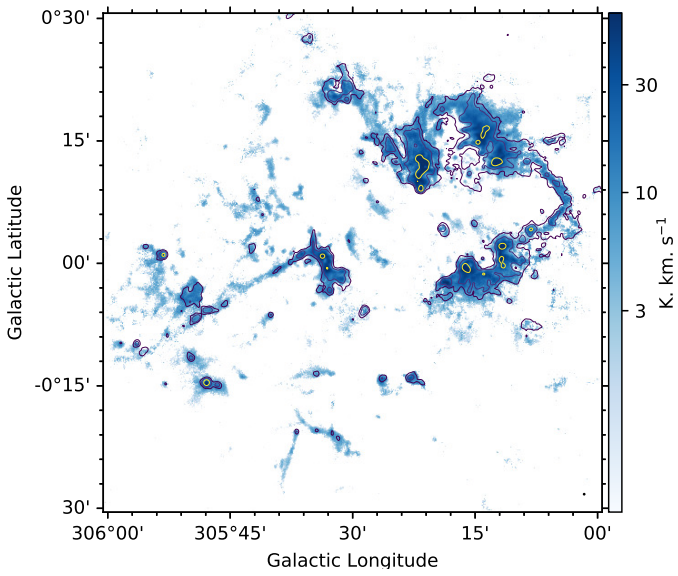

Fig. 3. ^{13}CO(3-2) moment-0 map of the G305 region. Overlaid are the contours of ATLASGAL corresponding to intensities 0.6, 1, and 3 Jy/beam.

GAL (Schuller et al. 2009; Contreras et al. 2013; Urquhart et al. 2014b) and CHIMPS (Rigby et al. 2016) surveys.

The Galactic clumps derived from the ATLASGAL survey (Urquhart et al. 2018) have the advantage of having a resolution similar to that of the LAsMA data (19″). Additionally, there is a good agreement in the sensitivity between the ATLASGAL data and the ^{13}CO intensity map, as can be seen in Fig. 3. The sensitivity to column density of the two datasets is also very similar; LAsMA traces column densities down to $\log(N(H_2)[cm^{-2}] \sim 21.46$ (see Paper I) and ATLASGAL is sensitive to clumps with column densities down to $\log(N(H_2)[cm^{-2}] \sim 21.5$ (Schuller et al. 2009; Urquhart et al. 2018).

On the other hand, the CHIMPS survey uses the same spectral line (^{13}CO(3-2)) used in our survey, which makes the comparison of properties more straightforward; **however**, the clump extraction from the CHIMPS survey was done on a smoothed dataset of resolution ∼ 27″ (Rigby et al. 2019). Hence, in order to compare the properties of the G305 clumps with the CHIMPS Galactic clumps, we created an additional smoothed data cube and repeated in parallel all the analyses that follow. While creating this new dendrogram, a structure was considered independent only if it was at least the size of the new beam. All comparison of properties with the CHIMPS clumps shown in this paper are based on the smoothed data cube.

In order to compare the properties of G305 clumps with any Galactic sample, similar spatial scales are more important than similar angular resolution. Therefore, a distance-limited sample ($3.5 < d < 4.5$ kpc) of Galactic clumps was used for comparison with clumps in G305. All references to the Galactic sample of clumps in this paper implicitly imply this distance-limited sample. For the CHIMPS survey it is possible to choose a different range of distances to avoid smoothing our dataset in order to compare similar clump sizes, but this leads to fewer clumps in the CHIMPS sample (a factor of 1.5 fewer clumps). Therefore, the former method was adopted for comparison with the CHIMPS sample.

4. Extracting clumps: Dendrogram

The clump catalog was created using the dendrogram analysis developed by Rosolowsky et al. (2008). It decomposes the intensity data cube into a nested hierarchy of structures called leaves, branches, and trunks. The leaves are the highest lying structures (with the brightest intensity) in this hierarchy and they generally represent the resolution element achievable by the survey designs. They consist of a collection of isocontours that contain only one local maximum within them. Branches are the structures that contain other leaves and branches inside them and trunks are the largest contiguous structures at the bottom of this hierarchy. Trunks by definition could also be leaves that are single isolated structures without any parent structure. Hence each structure identified by `astrodendro` as either a leaf or a branch depending on whether it has a lower hierarchy of structures under it.

The dendrogram algorithm `astrodendro`[3] was run on the data cube in position-position-velocity (ppv) space. A lower limit (*min_value*) of $5\sigma_{noise}$ was set to avoid getting structures with peak intensity below the noise threshold. Additionally, a structure was considered independent only if its peak intensity differed by at least $5\sigma_{noise}$ from the nearest local maximum (*min_delta*). Each structure was required to have an area equal to the area of the beam to be considered real. In the velocity space a minimum width of four channels ($= 2\,\mathrm{km\,s^{-1}}$) was implemented to prune the dendrogram (i.e., to get rid of unwanted structures due to noise in the data). Figure 4 shows the resulting dendrogram of the ^{13}CO data cube. The branching shows the fragmentation of a cloud into smaller and denser clumps.

5. Catalog of clump properties

Once the dendrogram was created, the `astrodendro` package was used to create a catalog of some basic properties of all the

[3] astrodendro is a Python package for computing dendrograms of astronomical data (`http://www.dendrograms.org/`).

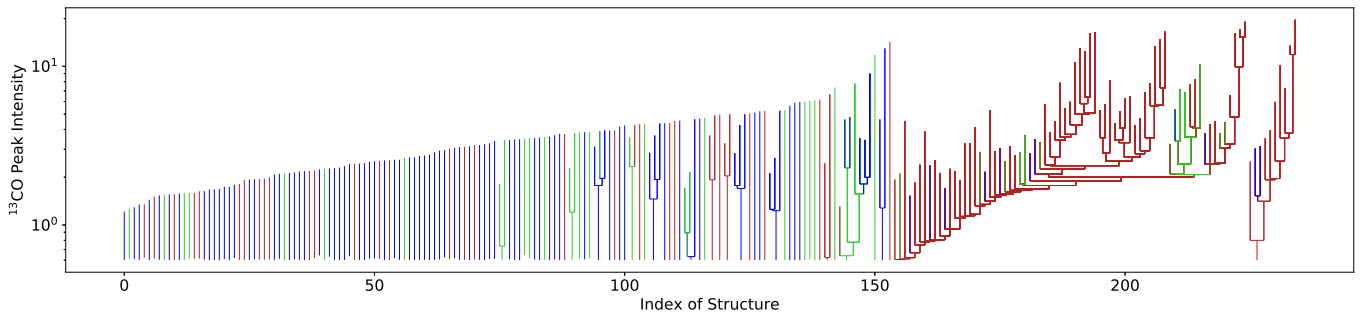

Fig. 4. Dendrogram of G305 on ^{13}CO spectral cube. The structures that show greater than ~ 67% overlap with the 8 μm mask (regions with 8 μm flux greater than 100 MJy/sr representing molecular gas influenced by feedback from the central star clusters in G305.) are colored red; those with partial overlap (between 10 - 67%) are colored green; and the structures with less than 10% overlap with the 8 μm mask are colored blue.

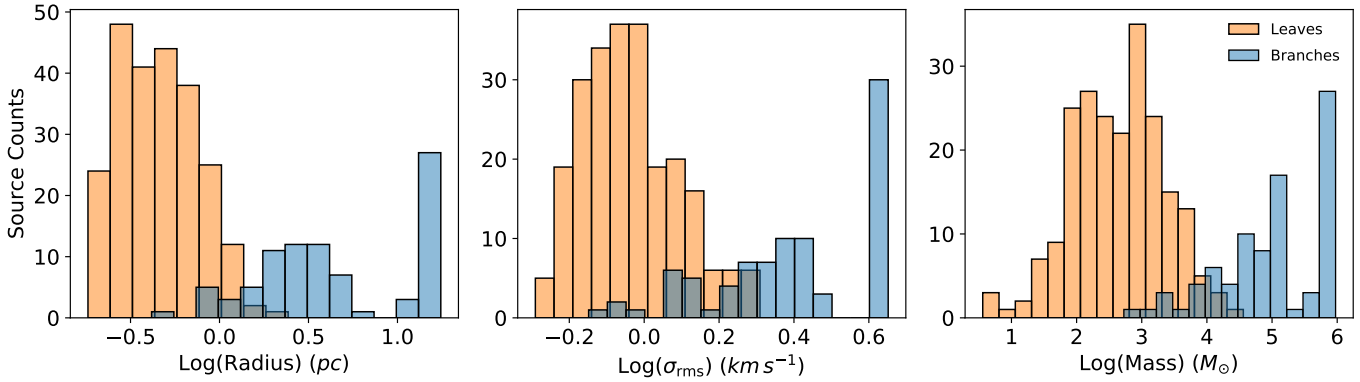

Fig. 5. Comparison of radii (left), velocity dispersions (center), and masses (right) of leaves and branches in G305.

structures. These include their positions, mean and RMS velocities, total fluxes, and the projections of their major and minor axes ($\sigma_{\rm maj}$ and $\sigma_{\rm min}$) on the position-position plane (Rosolowsky & Leroy 2006). The radius of the clumps is defined by $R_{\rm eq} = \eta * \sqrt{\sigma_{\rm maj} * \sigma_{\rm min}}$, where η is a factor that relates the radius of a spherical cloud to its one-dimensional RMS size $\sqrt{\sigma_{\rm maj} * \sigma_{\rm min}}$. For consistency with Solomon et al. (1987); Rosolowsky & Leroy (2006); Colombo et al. (2019); Rigby et al. (2019) we adopt the value $\eta = 1.91$. The velocity dispersion (σ_v) is calculated as the intensity weighted second moment of the velocity axis. The flux of the region is the sum (zeroth moment) of all the emission in the region. The physical radius of the clumps and their luminosities were calculated using $R_{\rm pc} = Rd$ and $L = Fd^2$, respectively, where $d = 3.8$ kpc is the distance to G305 (Clark & Porter 2004; Borissova et al. 2019).

Masses of the clumps were calculated using the column density maps. Section 4 of Paper I describes in detail how the column density map was obtained for the region. We present a brief summary of the method here. Assuming that ^{12}CO is optically thick, the excitation temperature T_{ex} of each pixel in the ppv space (hereafter voxel) was calculated under the assumption of local thermodynamic equilibrium (LTE). Then the ^{13}CO optical depth was derived for each voxel from the excitation temperature obtained from ^{12}CO and the ^{13}CO intensity. Subsequently, the ^{13}CO column density for each voxel was calculated using the derived excitation temperature and optical depth. Since the column density derived is only available for those pixels with a significant emission in ^{13}CO , all the properties calculated (and consequently all discussions about the clump properties) from here on are only applicable to the clumps extracted from the dendrogram of the ^{13}CO map of the region. As mentioned in Sect. 3, this has the added advantage of having a similar sensitivity to ATLASGAL data as well as using the same transition as the CHIMPS survey.

The column density over all the voxels corresponding to each clump in the dendrogram were added and the mass of the structure was then calculated using the equation

$$M = \mu\, m_p\, R_{13}^{-1} \sum_{lmv} N_{13}({\rm total})_{\rm lbv}\, \Delta{\rm x}\Delta{\rm y}, \quad (1)$$

where μ is the mean mass per H_2 molecule, taken to be 2.72, accounting for a helium fraction of 0.25 (`cite Allen 1973`), m_p is the mass of a proton, R_{13}^{-1} is the abundance ratio of H_2 compared with ^{13}CO, and Δx and Δy are the resolution elements (in parsec) calculated using the distance of the source and the resolution element. The conversion R_{13}^{-1} is calculated in two steps, and we adopt a ratio of R_{12}/R_{13} that varies as a function of galactocentric distance, as prescribed by Milam et al. (2005), and a value of $R_{12} = 8.5 \times 10^{-5}$ (Frerking et al. 1982) is adopted for all sources. The ratio R_{12}/R_{13} has a value of approximately 59.7 for the G305 galactocentric distance of 6.6 kpc.

The masses of the clumps and their radii were also used to calculate their density($n(H_2)$) and surface mass densities using

$$n(H_2) = 15.1 \times M/(4/3\,\pi R_{\rm eq}^3), \quad (2)$$

$$\Sigma = M/\pi\, R_{\rm eq}^2. \quad (3)$$

Table 1. Properties of the 20 randomly selected structures (leaves and branches) derived from the ^{13}CO dendrogram of G305. This table displays a small subset of the whole catalog.[a]

Catalog Index	Structure Type	x_c (°)	y_c (°)	Radius (pc)	v_{rms} (km s^{-1})	log(Lum) (K km s^{-1} pc^2)	log(Mass) ($M_\odot$)	α_{vir}	log($n(H_2)$) (cm^{-3})	log($\bar{F}_{8\,\mu m}$) (MJy/sr)
18	branch	305.284	0.161	13.8	4.0	3.54	5.77	0.26	2.9	2.36
24	branch	305.804	-0.235	2.5	1.9	2.18	4.37	0.25	3.76	1.74
28	branch	305.222	0.119	10.7	4.5	3.3	5.54	0.43	3.0	2.39
53	branch	305.284	0.161	13.8	4.0	3.54	5.77	0.26	2.91	2.36
60	branch	305.246	-0.014	2.5	1.9	2.48	4.72	0.12	4.09	2.52
67	leaf	305.231	-0.025	0.7	0.7	1.52	3.77	0.05	4.7	2.35
84	branch	305.865	-0.045	4.2	1.4	2.43	4.54	0.17	3.21	2.02
86	leaf	305.612	0.143	0.8	1.8	0.99	3.69	0.35	4.58	1.8
116	leaf	305.175	0.254	0.5	0.9	0.01	1.66	5.67	3.21	2.15
119	leaf	305.223	0.324	0.6	1.0	0.54	2.68	0.82	3.95	2.06
123	leaf	305.928	-0.1	0.3	1.2	0.05	2.02	2.35	4.33	1.7
129	leaf	305.208	0.141	0.6	0.7	0.72	2.88	0.31	4.09	2.1
137	branch	305.576	-0.006	4.4	2.1	2.72	4.91	0.17	3.53	2.4
159	branch	305.361	0.2	1.0	2.3	1.99	4.23	0.21	4.81	2.99
187	branch	305.564	0.002	2.3	1.8	2.42	4.61	0.12	4.09	2.53
249	leaf	305.67	0.025	0.6	1.5	0.71	2.74	1.62	3.95	2.29
267	leaf	305.552	-0.055	0.7	1.2	1.16	3.47	0.23	4.49	2.29
272	leaf	305.681	0.307	0.9	0.9	1.14	3.65	0.13	4.3	1.91
292	leaf	305.493	0.01	0.3	0.8	-0.28	1.84	1.71	4.11	1.82
321	leaf	305.28	-0.153	0.6	1.0	0.32	1.86	5.77	3.1	1.76

[a] The full table is available electronically.

Here M is in $M_\odot$, R_{eq} is in pc, $n(H_2)$ is in cm^{-3}, and Σ is in $M_\odot$/pc^2. The factor of 15.1 is used to convert the density to appropriate units.

The dynamical state of the clumps (i.e., whether they are gravitationally stable, collapsing, or dissipating) is examined using the virial theorem. With only gravitational forces the virial theorem reads $2K + \Omega = 0$, where K is the kinetic energy and Ω is the gravitational energy. The virial parameter is defined as the ratio of the virial mass of a spherically symmetric cloud to its total mass:

$$\alpha_{vir} = \frac{3\sigma_v^2 R_{eq}}{GM}. \quad (4)$$

Here σ_v is the velocity dispersion of the clump and G is the gravitational constant. This is the definition used by MacLaren et al. (1988). We also assume a spherical density distribution $\rho(r) = 1/r^2$. In the absence of pressure supporting the cloud $\alpha_{vir} < 1$ means that the cloud is gravitationally unstable and collapsing, whereas $\alpha_{vir} > 2$ means that the kinetic energy is higher than the gravitational energy and that the cloud is dissipating. A value of α_{vir} between 1 and 2 is interpreted as an approximate equilibrium between the gravitational and kinetic energies. A cloud undergoing gravitational collapse can also show $\alpha_{vir} \sim 2$ as the rapid infall can manifest as a large velocity dispersion (Kauffmann et al. 2013).

The dendrogram resulted in a total of 337 structures of which 235 (69.73%) are leaves and 102 (30.27%) are branches. Figure 5 shows the properties of the leaves and branches to demonstrate their differences. Table 1 shows 20 randomly selected clumps in the G305 giant molecular cloud.

6. Effect of feedback on G305 clumps

The radiation and ionization front from the OB stars in the central cavity can effect the masses as well as the velocity dispersion of the clumps in G305. It can inject turbulence which should manifest as broad linewidths of the clumps. It can also compress and destabilize the clumps resulting in an increase in their surface mass densities.

6.1. Insufficient velocity resolution

Before we investigate the effects of feedback on the linewidths of clumps we first calculate whether we posses enough resolution in velocity to discern any differences that might occur in their linewidths due to feedback. Assuming that the observed width of a clump is solely attributed to its turbulence, we can write the turbulent pressure in a clump as

$$P_{NT} = n(H_2) m_{H_2} \sigma^2 / k\,, \quad (5)$$

where k is the Boltzmann's constant and σ is its velocity dispersion in one dimension. If all the turbulent pressure is being delivered to the clumps by the stars in the center of G305, then $P_{star} = P_{NT}$, where P_{star} is given by

$$P_{star} = Q(H^0)\langle h\nu\rangle / 4\pi d^2 c\,, \quad (6)$$

where $Q(H^0)$ is the number of H ionizing photons per second emitted by the stars, $\langle h\nu\rangle$ is the mean photon energy of an O-star ($\sim$ 15eV Pellegrini et al. (2007)), d is the distance of the star (cluster) from the cloud surface, and c is the speed of light. It is tricky to calculate P_{star} given that the distance to each cloud is different and that the stars are not localized. However, in order to obtain an upper limit on the value of P_{star} we assume the total ionizing radiation of Danks 1 and 2 combined. In Danks 1 we have two O8-B3 and one O8-B3I star for which we adopt the

value corresponding to three O8V stars from Table 2 in Panagia (1973). Similarly, we use O4V values for the three O4-6 stars, O6V values for the one O6-8 and two O6-8If stars. For the three WNLh stars we adopt the value corresponding to WN-3w from Table 2 in Crowther (2007). Therefore for Danks 1 we have a maximum ionizing flux equal to 3.67×10^{50} s^{-1}. For Danks 2, there are three O6 (O6-8), four O8 (O8-9 / O8-B3I), and one WC7 (WC7-8) stars (we have ignored the F8-G1 star). Assuming all these belong to class V, we obtain 8.03×10^{49} s^{-1}. Hence, Danks 1 and 2 have a combined maximum Lyc photon output of 4.473×10^{50} s^{-1}. The value of d is assumed to be 4 pc, which is approximately the closest distance of clumps in the northern and southern complex to the Danks cluster. Plugging these into Eq. 6, we obtain a value of $P_{\rm star} \sim 1.36 \times 10^6$ K cm^{-3}. This corresponds to a velocity dispersion of $\sigma = 1.06$ km s^{-1} given an H_2 density of 10^4 cm^{-3}. Since our dataset has a velocity resolution of 0.5 km s^{-1}, it is difficult to discern the effects of feedback on the velocity dispersion of the clumps, which will realistically be much smaller than $\sim$ 1 km s^{-1}. The linewidths of the clumps were plotted as a function of the 8 μm flux and no dependence was observed between the linewidths of the clumps at the highest hierarchical level (leaves) and the strength of the feedback on the clumps supporting our claim. These results are presented in the Appendix (Fig. A.1) as they do not provide any new information to the question we are trying to answer in this paper.

6.2. Surface mass densities of clumps vs 8 μm

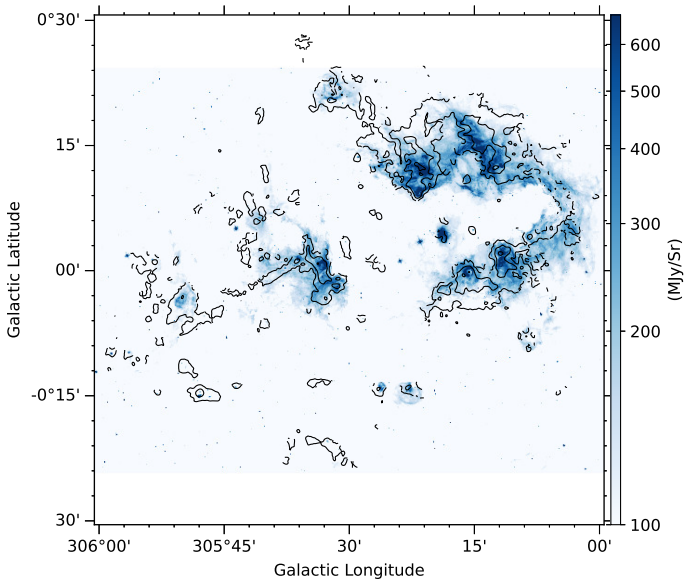

Fig. 6. GLIMPSE 8 μm map of the G305 regions. The black contours correspond to the ^{13}CO J=3–2 integrated intensities of 5(5σ), 20(20σ), and 80(80σ) K km s^{-1}.

In Paper I we discussed the role of the Galactic Legacy Infrared Mid-Plane Survey Extraordinaire (GLIMPSE: Benjamin et al. 2003; Churchwell et al. 2009) 8 μm continuum map as an indicator of feedback strength. As a proxy to the strength of feedback on each clump, we calculated the average 8 μm flux over each clump. For this, a mask was extracted for each structure by projecting it onto the position-position plane and the 8 μm flux was averaged over the mask. Table 1 also shows the mean 8 μm flux associated with each structure.

A significant issue with this analysis is that the 8 μm map is a two-dimensional projection on the plane of G305 and hence it is possible for clumps to appear to be affected by feedback because of their projection. In order to test whether the associated 8 μm fluxes actually correspond to the clumps we first compared the morphology of the 8 μm emission with the ^{13}CO integrated intensity map. Figure 6 shows the GLIMPSE map with the ^{13}CO integrated intensity contours overlaid. There is very good correlation between the two. So, we safely assume here that all the 8 μm emission is originating in G305. We then investigated whether any leaves in the dendrogram had the same position but different velocities along the line of sight. We found only about 1% of the leaves ($\sim$ 7% if branches are included) had positions within one beam size distance of another leaf (or branch). Additionally, Hindson et al. (2013) looked at the morphology of the molecular gas emission and argued that the G305 complex has a flattened geometry instead of a spherical structure. Taking these factors into consideration, we could safely ignore the effects of projection on the associated 8 μm fluxes for the clumps.

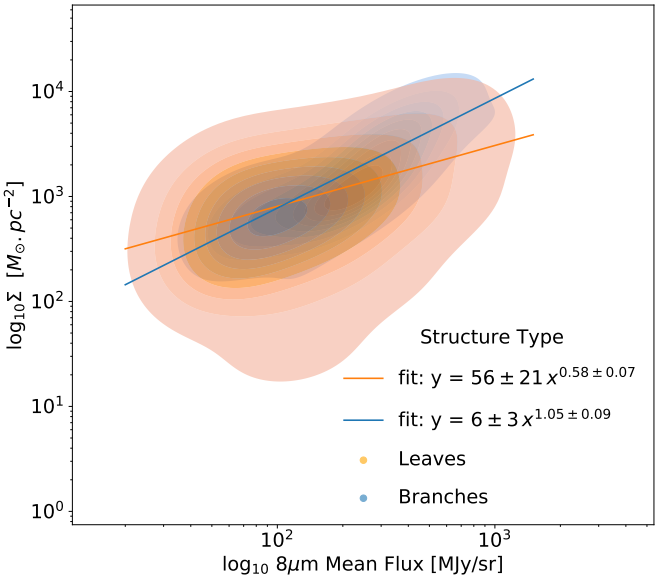

Fig. 7. Surface mass density of clumps in G305 as a function of 8μm flux. The orange and blue lines show the results of a power law fit to these quantities for leaves and branches respectively.

Figure 7 shows the two-dimensional kernel density estimate (KDE) distribution of the clump surface mass density as a function of 8 μm flux. The leaves and branches of the dendrogram have been plotted separately. We observe that the surface mass density of the clumps increases with increasing 8 μm flux, indicating that in regions of stronger feedback the clumps are more massive. A power law fit between the two quantities resulted in the following relation between them for leaves and branches:

$$\Sigma_l = 56 \pm 21\, \mathrm{F}_{8\mu m}^{0.58\pm0.07}, \quad (7)$$

$$\Sigma_b = 6 \pm 3\, \mathrm{F}_{8\mu m}^{1.05\pm0.09}. \quad (8)$$

Here Σ_l and Σ_b are the surface mass densities of the leaves and branches, respectively, and $\mathrm{F}_{8\mu m}$ is the average 8μm flux incident on the structure. A positive correlation between the surface mass density of the clumps and the incident 8 μm flux is indicative of triggering in G305. In the redistribution scenario we would have

expected no correlation between the two quantities, and in case of the disruptive scenario we should have observed a negative correlation.

6.3. Inside and outside the feedback zone

The analysis described in the previous subsection motivated us to follow an approach similar to that presented in Paper I. Based on an 8 μm threshold, a feedback zone was defined as the pixels with 8 μm flux larger than the threshold. The value of this threshold was chosen to be 100 MJy/sr corresponding to the first inflection point in Fig. 15 of Paper I. We believe this contour corresponds to the isosurface where the stellar feedback gets deposited first. Then each clump was assigned a tag depending on the extent of its overlap with the feedback zone. Clumps with more than 67% overlap with the feedback zone were tagged "Mostly Inside"; those with an overlap between 10 and 67% were tagged "Partly Inside", and those with less than 10% overlap with the feedback zone were tagged "Outside". This classification is not based on any physics, but in order to aid the explanation that is to follow. Using this classification results in 95 leaves (40.4%) that were mostly inside, 40 leaves (17.0%) were partly inside, and 100 leaves (42.6%) were outside the feedback zone. The same was done with branches, which led to 75 branches (73.6%) mostly inside, 14 (13.7%) partly inside, and 13 (12.7%) outside the feedback zone.

Figure 8 shows the probability density distribution of the surface mass densities of the structures based on their tags. There is a clear trend of increasing surface mass density in association with the overlap with the feedback zone. A Kolmogorov–Smirnov (KS) test (Kolmogorov 1933; Smirnov 1939) was performed on the pairs of these distributions to test the hypothesis that these samples of surface mass densities have been taken from the same population. In the case of leaves only the mostly inside and the outside samples rejected the null hypothesis (p-value = 0.0011%). The other pair of samples did not reject the null hypothesis (p-value = 0.12 for mostly inside vs partly inside and 0.18 for partly inside vs outside). The branches in the mostly inside category were significantly different from those in the mostly outside category (p-value<< 0.0013), but not from the partly inside branches (p-value=0.002). These findings support the C&C model, which predicts that the clumps are more massive under feedback.

Another prediction of the C&C model is that there will be a higher level of fragmentation in the cloud being affected by feedback. To test this we color-coded the structures of the dendrogram in Fig. 4 based on their tags. We observe that the largest hierarchical structure almost completely lies mostly inside the feedback zone with some structures being partly inside. The structures outside the feedback zone show very little fragmentation. This is further support for the C&C model in the case of G305.

7. G305 versus Galactic clumps

We have seen so far that feedback from the central cluster of stars has a significant impact on the clumps in G305. This suggests that the properties of the clumps in G305 should be significantly different from the average sample of Galactic clumps. In order to test this we compared the properties of G305 clumps with those of the Galactic sample of clumps derived from ATLASGAL and CHIMPS.

Figure 9 shows the distribution of different properties of clumps in G305 along with the Galactic sample derived for both

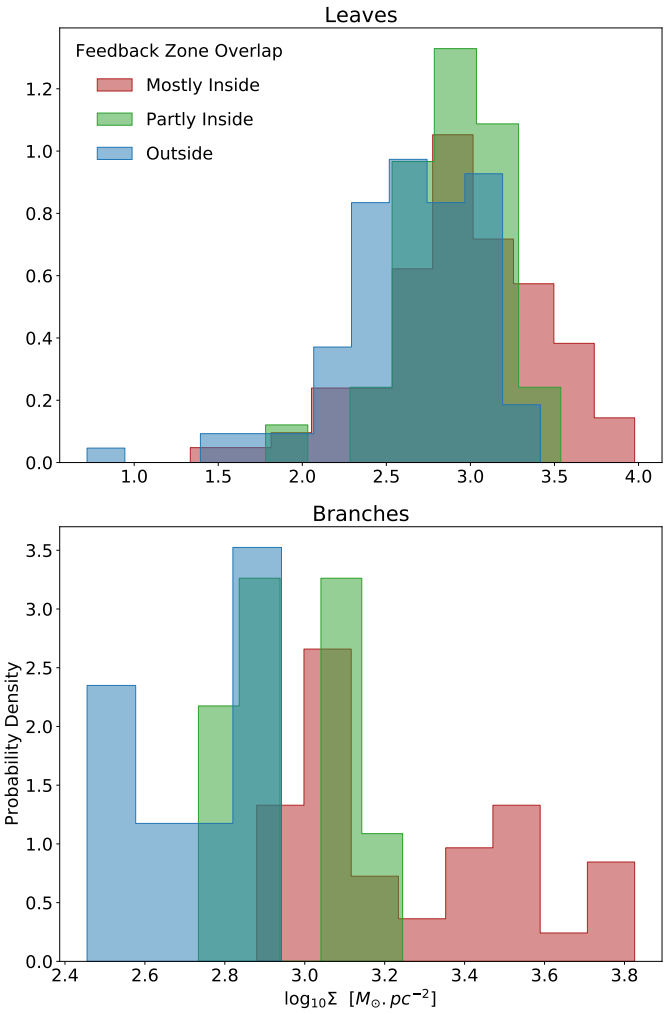

Fig. 8. Histogram of the probability density of surface mass densities of leaves (top) and branches (bottom) based on their overlap with the feedback zone defined using an 8 μm threshold of 100 MJy/sr.

ATLASGAL clumps (Urquhart et al. 2018; Contreras et al. 2013) and CHIMPS clumps (Rigby et al. 2019). In order to compare the clumps properties only the CHIMPS clumps with the highest reliability flag (= 3) were considered (Rigby et al. 2019).

The radii of the clumps in G305 are smaller than the CHIMPS clumps. This could be because of the differences in the clump extraction method used by (Rigby et al. 2019). Compared to the dendrogram clumps, the `FELL-WALKER` method (Berry 2015) would have slightly larger areas. In comparison to ATLASGAL, the G305 clumps appear to have a different distribution, but this difference is not significant, as confirmed by performing a KS test on the radius of the two populations (p-value=0.0022).

The linewidths of the G305 clumps appear to have a different distribution from the ATLASGAL and CHIMPS samples. A KS test performed on the linewidths of G305 clumps with the two Galactic samples resulted in a p-value<< 0.0013 for both the populations confirming this. The ATLASGAL survey used the NH_3 spectral line to estimate linewidths, whereas the CHIMPS survey used the same line used in our observations and hence this comparison is more straightforward. We observe the

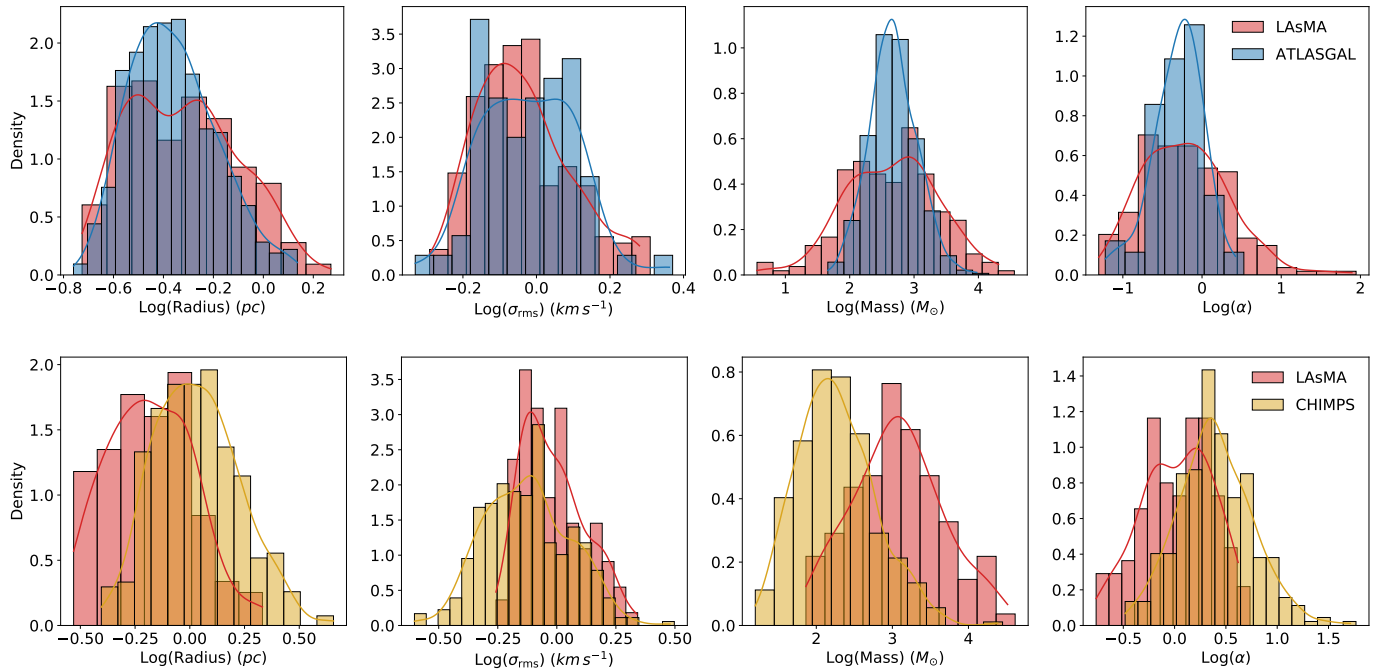

Fig. 9. Comparison of properties of LAsMA clumps in G305 with a Galactic sample derived from ATLASGAL (top panel) and CHIMPS (bottom panel) surveys. The solid lines overlaid in matching colors show the KDE of the distribution of the corresponding properties.

linewidths to be higher in case of G305 clumps when compared to the CHIMPS population of Galactic clumps.

The G305 clumps show a much broader distribution of masses compared to ATLASGAL. The greater sensitivity of our observations would explain why we see more clumps of lower masses compared to ATLASGAL as these would not be detected in the ancillary survey. In comparison to the CHIMPS population of clumps, the masses of G305 clumps are much higher. G305 also has a higher fraction of heavier clumps compared to the ATLASGAL sample. This is indicative of some form of triggering. A KS test on the masses of the two populations resulted in a p-value << 0.0013 for masses of G305 clumps compared to the Galactic sample (for both ATLASGAL and CHIMPS populations) indicating that the G305 clumps are significantly different from the Galactic average.

The last panel in Fig. 9 shows the distribution of virial parameters of the G305 clumps. We see a broader distribution when compared to ATLASGAL clumps. A large proportion of clumps in G305 appear to have $\alpha_{\rm vir}$ << 2. According to Kauffmann et al. (2013), this is indicative of high mass star formation in G305. We also see a much higher fraction of clumps in G305 with $\alpha_{\rm vir}$ >> 2, which may be indicative of turbulence disrupting and dissipating clumps. Interestingly, the smoothed dendrogram does not have clumps with very high $\alpha_{\rm vir}$ values. This could be attributed to the bias towards larger structures in the smoothed dataset leading to more clumps with heavier masses. A KS test on the virial parameters of the G305 and Galactic clumps indicated these properties being drawn from significantly different populations (p-value<< 0.0013).

Triggering in G305

Proving that triggering is responsible for enhanced star formation is a difficult task. Often it is done by looking at morphological signposts such as star formation at the rim of the expanding shells of HII regions (Deharveng et al. 2005; Zavagno et al. 2005; Urquhart et al. 2007; Thompson et al. 2012; Kendrew et al. 2012; Palmeirim et al. 2017). In G305, Hindson et al. (2013) looked at star formation in different phases and compared their distribution in the complex to suggest that the most likely case of triggering is the C&C process. However, they did not find any conclusive evidence that the star formation happening in G305 has been triggered. They calculated the time needed for the gas to fragment into stars and suggested that while in some cases the age of the triggering stars was old enough to be responsible for the stars in their vicinity to be triggered. In many other cases, the stars responsible for triggering may not be old enough to drive the formation of the HII and UC HII regions. However, the fragmentation timescale estimates were based on assumptions about the initial ambient atomic density and the Lyman continuum photon rate, both of which are difficult to measure, making their suggestions inconclusive. So far in this paper we have explored whether the feedback from the stars is indeed triggering star formation in G305 by looking at their impact on the clumps which are the reservoirs of the new generation of stars.

The luminosity-to-mass ratio (L/M) of clumps is a good indicator of the evolutionary stage in star formation (see Molinari et al. 2008; Urquhart et al. 2018). A higher star-forming efficiency would mean that more clumps are in more evolved stages of forming stars, which would lead to a flatter cumulative distribution function of their L/M. In G305, if the clumps are simply being moved around without any effect on their star-forming efficiency, then the L/M distribution of the clumps in G305 should not vary significantly from the Galactic average. Figure 10 shows the cumulative distribution function (CDF) of the L/M for the ATLASGAL clumps in G305 compared to that of the the overall ATLASGAL Galactic sample. All the L/M values were taken from ATLASGAL as the calculation of the luminosity is quite different between our dataset and ATLASGAL. Consequently, comparing the L/M of clumps from our data with that of the

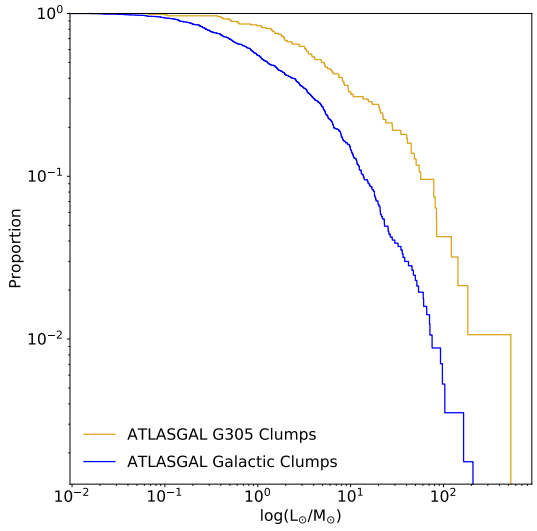

Fig. 10. CDF of L_{clumps}/M_{clumps} in G305 compared to that of the ATLASGAL Galactic clumps.

ATLASGAL clumps would not have been straightforward. The clumps in G305 show significantly higher L/M values than the Galactic average, as is shown by the CDF. A KS test on the two clump samples returned a p-value<< 0.0013. Therefore, the null hypothesis is quite overwhelmingly rejected indicating that the clumps in G305 show higher star-forming efficiency compared to the Galactic average. This rules out the redistribution and disruption scenarios. These clumps may not have a one-to-one correspondence with the ^{13}CO clumps derived in the previous sections, but that does not negate the validity of the finding here.

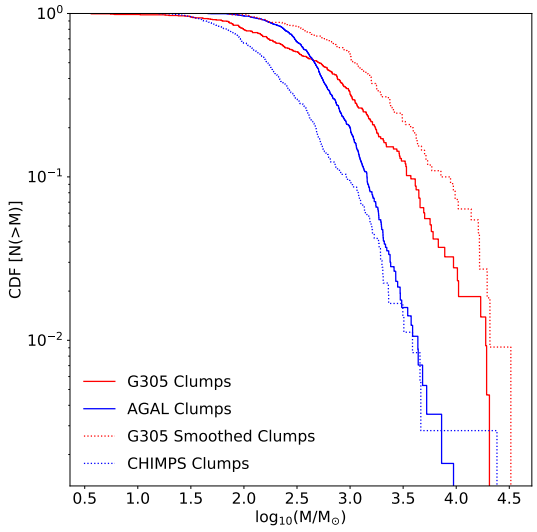

Fig. 11. CDF of LAsMA clump masses in G305 compared to that of the Galactic clump sample from ATLASGAL and CHIMPS.

Finally, in the case of triggering, if C&C is the dominant mechanism in play then we would observe more massive clumps as C&C causes the clump to accumulate mass (Whitworth et al. 1994; Deharveng et al. 2005). Figure 11 shows the CDF of the clump masses in G305 compared to the Galactic average. In addition to the ATLASGAL clumps, we also included those from CHIMPS. The method used to measure the clump properties in our paper is identical to that used by Rigby et al. (2019). Figure 11 shows the CDF of clump masses in G305 compared to the Galactic sample taken from ATLASGAL as well as CHIMPS. For both cases the clumps in G305 show a much flatter CDF than the Galactic average. A KS test between G305 clumps and ATLASGAL (CHIMPS) clumps yielded a p-value<< 0.0013 again rejecting the null hypothesis that the G305 LAsMA clumps and the Galactic ATLASGAL (CHIMPS) clumps belong to the same distribution. The flatter slope of the clump mass CDF of G305 proves that C&C is the dominant mechanism inside the GMC.

8. Summary

We observed the G305 region with the LAsMA receiver on the APEX telescope using the ^{12}CO (3−2) and ^{13}CO (3−2) lines in order to test the effect of feedback from the central cluster of stars on the clump properties.

We decomposed the molecular cloud into clumps using the Dendrogram analysis on the ^{13}CO data cube. We followed up by creating a catalog of clump properties. We tested the effect of feedback on two main clump properties, namely linewidths and surface mass densities. Using the 8 μm emission map of the region as a proxy to feedback strength, we examined the correlation of the surface mass densities of the clumps with the incident average 8 μm flux. We then masked the feedback zone based on an 8 μm flux threshold of 100 MJy/sr. The extent of overlap of each clump with the feedback zone was used to determine whether it was mostly inside, partly inside, or outside the feedback zone. The properties of these three populations of clumps were separately studied. We followed this up with a comparison of the properties of clumps in G305 as a whole to a distance-limited sample of Galactic clumps taken from ATLASGAL and CHIMPS surveys assuming that the Galactic sample of clumps are similar to a population of clumps that are quiescent. The cumulative distribution function (CDF) of the masses as well as the L/M ratios of the clumps (the latter having been derived entirely from ATLASGAL data) in G305 were obtained and compared to that of the Galactic average. We summarize our main findings below:

- Our data do not possess enough velocity resolution to discern the effect of feedback on the linewidths of the clumps.
- The surface mass densities of the clumps in the region are positively correlated to the incident average 8 μm flux.
- The surface mass densities of the clumps mostly inside the feedback zone are the highest, followed by those of the clumps partly inside and then outside the feedback zone, indicating that feedback is triggering their star-forming ability.
- Clumps inside the feedback zone show a much higher level of fragmentation than those partly inside or outside it.
- The probability density function (PDF) of the properties of G305 clumps are significantly different than those of the clumps derived from a distance-limited Galactic sample of clumps indicating clear evidence of triggering.
- The CDFs of the masses and the L/M ratios of the clumps in G305 are significantly flatter than those of the Galactic average. This is strong evidence for triggering (more specifically the C&C mechanism) being the dominant mechanism in G305, not redistribution or dispersion.

Therefore, we obtain multiple pieces of evidence demonstrating that the feedback from the central cluster of stars in G305 is triggering the collapse of the molecular cloud complex.

Acknowledgements. We thank the staff of the APEX telescope for their assistance in observations. This work acknowledges support by The Collaborative Research Council 956, sub-project A6, funded by the Deutsche Forschungsgemeinschaft (DFG). This research made use of astrodendro, a Python package to compute dendrograms of Astronomical data (http://www.dendrograms.org/). Data handling in this work has been done using the `Astropy` python package (Astropy Collaboration et al. 2013, 2018). Parts of this work are based on observations made with the Spitzer Space Telescope, which is operated by the Jet Propulsion Laboratory (JPL), California Institute of Technology under a contract with NASA. This publication also made use of data products from the Midcourse Space Experiment. Processing of the data was funded by the Ballistic Missile Defense Organization with additional support from NASA Office of Space Science. This research has also made use of the NASA/ IPAC Infrared Science Archive, which is operated by the JPL, under contract with NASA.

References

Astropy Collaboration, Price-Whelan, A. M., Sipőcz, B. M., et al. 2018, AJ, 156, 123
Astropy Collaboration, Robitaille, T. P., Tollerud, E. J., et al. 2013, A&A, 558, A33
Benjamin, R. A., Churchwell, E., Babler, B. L., et al. 2003, PASP, 115, 953
Berry, D. S. 2015, Astronomy and Computing, 10, 22
Bertoldi, F. 1989, ApJ, 346, 735
Bertoldi, F. & McKee, C. F. 1990, ApJ, 354, 529
Blitz, L. & Stark, A. A. 1986, ApJ, 300, L89
Borissova, J., Roman-Lopes, A., Covey, K., et al. 2019, AJ, 158, 46
Churchwell, E., Babler, B. L., Meade, M. R., et al. 2009, PASP, 121, 213
Clark, J. S. & Porter, J. M. 2004, A&A, 427, 839
Colombo, D., Rosolowsky, E., Duarte-Cabral, A., et al. 2019, MNRAS, 483, 4291
Contreras, Y., Schuller, F., Urquhart, J. S., et al. 2013, A&A, 549, A45
Crowther, P. A. 2007, ARA&A, 45, 177
Dale, J. E., Bonnell, I. A., & Whitworth, A. P. 2007, MNRAS, 375, 1291
Davies, B., Clark, J. S., Trombley, C., et al. 2012, MNRAS, 419, 1871
de Geus, E. J. 1992, A&A, 262, 258
Deharveng, L., Schuller, F., Anderson, L. D., et al. 2010, A&A, 523, A6
Deharveng, L., Zavagno, A., & Caplan, J. 2005, A&A, 433, 565
Elmegreen, B. G. & Lada, C. J. 1977, ApJ, 214, 725
Faimali, A., Thompson, M. A., Hindson, L., et al. 2012, MNRAS, 426, 402
Frerking, M. A., Langer, W. D., & Wilson, R. W. 1982, ApJ, 262, 590
Fukui, Y., Habe, A., Inoue, T., Enokiya, R., & Tachihara, K. 2021, PASJ, 73, S1
Green, J. A., Caswell, J. L., Fuller, G. A., et al. 2009, MNRAS, 392, 783
Green, J. A., Caswell, J. L., Fuller, G. A., et al. 2012, MNRAS, 420, 3108
Güsten, R., Baryshev, A., Bell, A., et al. 2008, in Society of Photo-Optical Instrumentation Engineers (SPIE) Conference Series, Vol. 7020, Proc. SPIE, 702010
Güsten, R., Nyman, L. Å., Schilke, P., et al. 2006, A&A, 454, L13
Heyer, M., Krawczyk, C., Duval, J., & Jackson, J. M. 2009, ApJ, 699, 1092
Hindson, L., Thompson, M. A., Urquhart, J. S., Clark, J. S., & Davies, B. 2010, MNRAS, 408, 1438
Hindson, L., Thompson, M. A., Urquhart, J. S., et al. 2012, MNRAS, 421, 3418
Hindson, L., Thompson, M. A., Urquhart, J. S., et al. 2013, MNRAS, 435, 2003
Kauffmann, J., Pillai, T., & Goldsmith, P. F. 2013, ApJ, 779, 185
Kendrew, S., Simpson, R., Bressert, E., et al. 2012, ApJ, 755, 71
Kessel-Deynet, O. & Burkert, A. 2003, MNRAS, 338, 545
Kolmogorov, A. 1933, Inst. Ital. Attuari, Giorn., 4, 83
Krumholz, M. R., Bate, M. R., Arce, H. G., et al. 2014, in Protostars and Planets VI, ed. H. Beuther, R. S. Klessen, C. P. Dullemond, & T. Henning, 243
Lada, E. A. 1992, ApJ, 393, L25
Lee, H.-T. & Chen, W. P. 2007, ApJ, 657, 884
Leistra, A., Cotera, A. S., Liebert, J., & Burton, M. 2005, AJ, 130, 1719
Lumsden, S. L., Hoare, M. G., Urquhart, J. S., et al. 2013, ApJS, 208, 11
MacLaren, I., Richardson, K. M., & Wolfendale, A. W. 1988, ApJ, 333, 821
Mauerhan, J. C., Van Dyk, S. D., & Morris, P. W. 2011, AJ, 142, 40
Mazumdar, P., Wyrowski, F., Colombo, D., et al. 2021, A&A, 650, A164
Milam, S. N., Savage, C., Brewster, M. A., Ziurys, L. M., & Wyckoff, S. 2005, ApJ, 634, 1126
Molinari, S., Pezzuto, S., Cesaroni, R., et al. 2008, A&A, 481, 345
Motte, F., Bontemps, S., & Louvet, F. 2018, ARA&A, 56, 41
Nagakura, T., Hosokawa, T., & Omukai, K. 2009, MNRAS, 399, 2183
Palmeirim, P., Zavagno, A., Elia, D., et al. 2017, A&A, 605, A35
Panagia, N. 1973, AJ, 78, 929
Pellegrini, E. W., Baldwin, J. A., Brogan, C. L., et al. 2007, ApJ, 658, 1119
Price, S. D., Egan, M. P., Carey, S. J., Mizuno, D. R., & Kuchar, T. A. 2001, The Astronomical Journal, 121, 2819
Rigby, A. J., Moore, T. J. T., Eden, D. J., et al. 2019, A&A, 632, A58
Rigby, A. J., Moore, T. J. T., Plume, R., et al. 2016, MNRAS, 456, 2885
Rosolowsky, E. & Leroy, A. 2006, PASP, 118, 590
Rosolowsky, E. W., Pineda, J. E., Kauffmann, J., & Goodman, A. A. 2008, ApJ, 679, 1338
Schuller, F., Menten, K. M., Contreras, Y., et al. 2009, A&A, 504, 415
Shara, M. M., Moffat, A. F. J., Gerke, J., et al. 2009, AJ, 138, 402
Smirnov, N. V. 1939, Bull. Math. Univ. Moscou, 2, 3
Solomon, P. M., Rivolo, A. R., Barrett, J., & Yahil, A. 1987, ApJ, 319, 730
Thompson, M. A., Urquhart, J. S., Moore, T. J. T., & Morgan, L. K. 2012, MNRAS, 421, 408
Ulich, B. L. & Haas, R. W. 1976, ApJS, 30, 247
Urquhart, J. S., Figura, C. C., Moore, T. J. T., et al. 2014a, MNRAS, 437, 1791
Urquhart, J. S., König, C., Giannetti, A., et al. 2018, MNRAS, 473, 1059
Urquhart, J. S., Moore, T. J. T., Csengeri, T., et al. 2014b, MNRAS, 443, 1555
Urquhart, J. S., Thompson, M. A., Morgan, L. K., et al. 2007, A&A, 467, 1125
Whitworth, A. P., Bhattal, A. S., Chapman, S. J., Disney, M. J., & Turner, J. A. 1994, MNRAS, 268, 291
Zavagno, A., Deharveng, L., Brand, J., et al. 2005, in Massive Star Birth: A Crossroads of Astrophysics, ed. R. Cesaroni, M. Felli, E. Churchwell, & M. Walmsley, Vol. 227, 346–351
Zinnecker, H. & Yorke, H. W. 2007, ARA&A, 45, 481

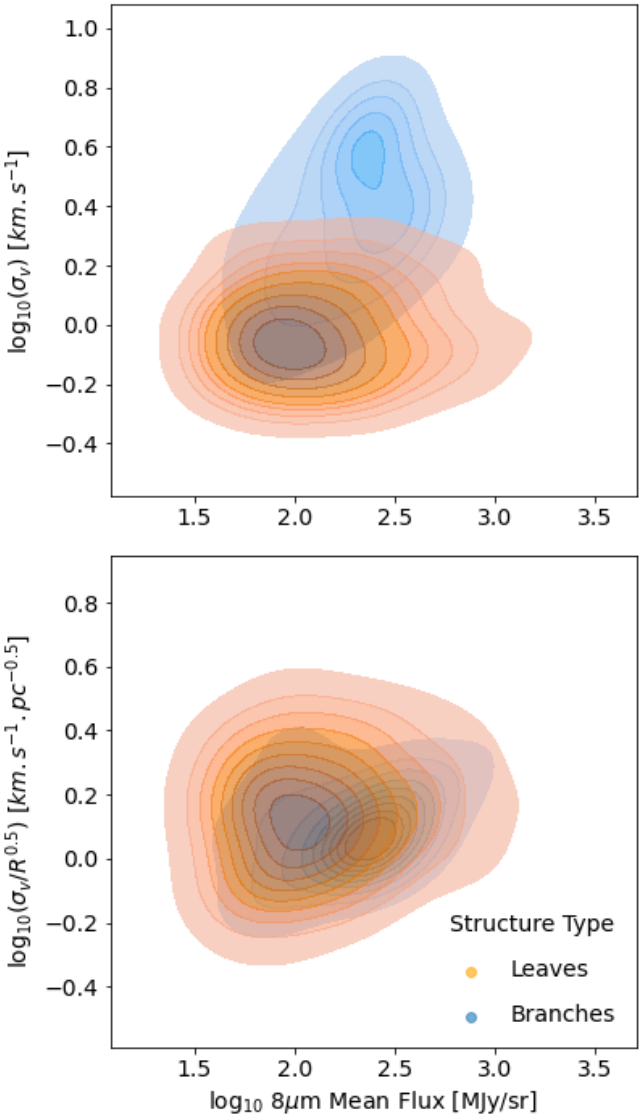

Fig. A.1. Linewidths for G305 clumps as a function of the incident 8 μm flux.

Appendix A: Velocity vs 8 μm

The linewidths of leaves (the highest hierarchical structures) show no dependence on the incident 8um flux, whereas the branches do show a positive correlation with the 8 μm flux. This could be the result of the size versus linewidth relationship of the clumps. When dividing the linewidths by the size of the structures (Heyer et al. 2009), the leaves still do not show any strong dependence of this property on the incident 8 μm flux, but the branches do show a weak positive dependence on the incident 8 μm flux. This indicates that at larger scales feedback from the stars injects turbulence into the GMC. Similar results were also seen in Paper I where the stacked spectra showed a positive dependence of their skewness and kurtosis on the incident 8um flux.